

# Q-Least Squares Reverse Time Migration with Viscoacoustic Deblurring Filters

Yuqing Chen<sup>1</sup> and Gaurav Dutta<sup>1</sup>

<sup>1</sup>King Abdullah University of Science and Technology (KAUST)

## ABSTRACT

Viscoacoustic least-squares reverse time migration (Q-LSRTM) linearly inverts for the subsurface reflectivity model from lossy data. Compared to the conventional migration methods, it can compensate for the amplitude loss in the migrated images because of the strong subsurface attenuation. However, the adjoint Q propagators used for backward propagating the residual data during Q-LSRTM are also attenuative. Thus, the inverted images from Q-LSRTM are often observed to have lower resolution when compared to the acoustic LSRTM images from acoustic data. To increase the resolution and accelerate the convergence of Q-LSRTM, we propose using viscoacoustic deblurring filters as a preconditioner for Q-LSRTM. These filters can be estimated by matching a simulated migration image to its reference reflectivity model. Numerical tests on synthetic and field data demonstrate that Q-LSRTM combined with viscoacoustic deblurring filters can produce images with higher resolution and more balanced amplitudes than images from acoustic RTM, acoustic LSRTM and Q-LSRTM when there is strong attenuation in the background medium. The proposed preconditioning method is also shown to improve the convergence rate of Q-LSRTM by more than 30 percent in some cases.

function (Schuster and Hu, 2000), sometimes denoted as a point spread function (PSF) (Jansson and Richardson, 1997), can be efficiently computed by invoking a layered-medium assumption localized around the trial image point. Therefore, the migration process can be approximated as a convolution between the reflectivity model and the migration Green's function. Using the above assumptions, the MD operation can be used as an approximation to the inverse of the Hessian and can sometimes be used as an alternative to least-squares migration (LSM) to mitigate migration artifacts.

Hu and Schuster (1998) and Hu et al. (2001) designed a migration deconvolution operator in the space-wavenumber domain to suppress the migration artifacts for poststack migration. Yu et al. (2006) extended the application of MD from poststack to prestack depth migration. Instead of using MD in the space-wavenumber domain, Guitton (2004) approximates the inverse of the Hessian in the space domain with a bank of matching filters. These filters are similar to deblurring filters and have been used as a preconditioner for conventional LSM (Aoki and Schuster, 2009). For multisource LSM, Dai et al. (2009) and Dai et al. (2011) used deblurring filters to reduce the crosstalk noise and accelerate the convergence of multisource LSM.

Previous works on MD assumed a lossless background medium. However, strong subsurface attenuation can significantly distort the amplitudes and phases of seismic waves (Aki and Richards, 1980). In this case, conventional acoustic reverse time migration (RTM) and least-squares reverse time migration (LSRTM) cannot correct for the attenuation loss.

To account for attenuation, Dai et al. (1994), Yu et al. (2002), Wang (2007) and Valenciano et al. (2011) used one-way wave-equation migration in the frequency domain for attenuation compensation. For reverse time migration, Zhang et al. (2010), Suh et al. (2012), Fletcher et al. (2012), Zhu et al. (2014) and Zhu and Harris (2015) pro-

## INTRODUCTION

Migration deconvolution (MD) is used to deblur migration images corrupted by artifacts due to coarse source and receiver sampling, limited aperture width, strong velocity contrasts, and uneven subsurface illumination (Hu et al., 2001). The MD filter assumes a homogeneous layered medium around the image point and a sufficiently wide recording aperture. In this case, the migration Green's

posed different viscoacoustic wave equations with separate controls over phase and amplitude to compensate for the attenuation loss. Dutta and Schuster (2014) and Sun et al. (2015) used iterative Q-LSRTM to successfully compensate for amplitude loss and phase distortion caused by attenuation. Viscoacoustic least-squares reverse time migration, also denoted as Q-LSRTM, has been shown to compensate for the attenuation loss and produce images with more balanced amplitudes and accurately positioned reflectors than standard migration techniques (Dutta and Schuster, 2014; Dai et al., 2015; Sun et al., 2016). However, the inverted images from Q-LSRTM sometimes have lower resolution when compared to the reference acoustic LSRTM images. This is because the adjoint Q propagators used for backpropagating the data residual during Q-LSRTM are also attenuative. Hence, a large number of least-squares iterations are required to get the desired uplift in the image quality, which makes the Q-LSRTM technique computationally expensive when compared to standard RTM.

To mitigate these problems, we propose using viscoacoustic deblurring filters as a preconditioner for Q-LSRTM. A reference reflectivity model is first constructed using a uniform distribution of point scatterers while the background velocity models is kept the same. The viscoacoustic data generated from these reference velocity and Q model are then migrated by viscoacoustic reverse time migration (Q-RTM) to obtain a reference migration image. The viscoacoustic deblurring filters are then estimated for different parts of the migration image by locally matching the simulated migration image to its reference reflectivity model using matched filters. These filters are then used as a preconditioner during the Q-LSRTM iterations. The estimation of these local filters can be done in parallel using MPI, which makes the preconditioning process very efficient. Results with these deblurring filters show a much faster convergence rate for Q-LSRTM and a much improved image for Q-RTM. These benefits only require the extra computational cost of constructing the deblurring filters, which is no more than one migration of the data.

This paper is divided into four sections. After the introduction, the second section presents the theory of Q-LSRTM with viscoacoustic deblurring filters. Numerical tests on synthetic and field data are then used to demonstrate the advantages of the proposed preconditioning method and the conclusions are in the last section.

## THEORY

Under the Born approximation, the observed data  $d(\mathbf{r}_s|\mathbf{r}_g, \omega)$  recorded at a receiver at  $\mathbf{r}_g$  and for a source at  $\mathbf{r}_s$  is given by

$$d(\mathbf{r}_s|\mathbf{r}_g, \omega) = \int_{V_0} w(\omega) G(\mathbf{r}_g|\mathbf{r}_0, \omega) G(\mathbf{r}_0|\mathbf{r}_s, \omega) m(\mathbf{r}_0) dV_0, \quad (1)$$

where  $\omega$  denotes angular frequency,  $w(\omega)$  denotes the frequency-domain representation of the second time derivative of the source wavelet,  $m(\mathbf{r}_0)$  is the reflectivity distribution at the subsurface location  $\mathbf{r}_0$  and  $V_0$  is the 3D integration volume.  $G(\mathbf{r}_g|\mathbf{r}_s, \omega)$  denotes the Green's function computed for background. Using a matrix-vector notation, equation 1 can also be written as

$$\mathbf{d} = \mathbf{L}\mathbf{m}_0, \quad (2)$$

where  $\mathbf{L}$  represents a linear modeling operator and  $\mathbf{m}_0$  is the subsurface reflectivity model. The migration image  $\mathbf{m}_{mig}$  is computed by applying a migration operator  $\mathbf{L}^T$  to the observed data and is represented by

$$\mathbf{m}_{mig} = \mathbf{L}^T \mathbf{d} = \overbrace{\mathbf{L}^T \mathbf{L}}^{\text{blurring operator}} \mathbf{m}_0. \quad (3)$$

Using Green's function notation, equation 3 can also be expressed as

$$m_{mig}(\mathbf{r}) = \int_{V_0} \int_{-\infty}^{\infty} d\omega \sum_g \sum_s w(\omega) w(\omega)^* G^*(\mathbf{r}_g|\mathbf{r}, \omega) G^*(\mathbf{r}|\mathbf{r}_s, \omega) \quad (4)$$

$$G(\mathbf{r}_g|\mathbf{r}_0, \omega) G(\mathbf{r}_0|\mathbf{r}_s, \omega) m(\mathbf{r}_0) dV_0, \\ = \int_{V_0} \Gamma(\mathbf{r}|\mathbf{r}_0) m(\mathbf{r}_0) dV_0,$$

where

$$\Gamma(\mathbf{r}|\mathbf{r}_0) = \int_{-\infty}^{\infty} d\omega \sum_g \sum_s w(\omega) w(\omega)^* G^*(\mathbf{r}_g|\mathbf{r}, \omega) G^*(\mathbf{r}|\mathbf{r}_s, \omega) \quad (5)$$

$$G(\mathbf{r}_g|\mathbf{r}_0, \omega) G(\mathbf{r}_0|\mathbf{r}_s, \omega).$$

Here,  $\Gamma(\mathbf{r}|\mathbf{r}_0)$  denotes the migration Green's function at location  $\mathbf{r} = (x, y, z)$  for a point scatterer at  $\mathbf{r}_0 = (x_0, y_0, z_0)$ .

Since the adjoint operator  $\mathbf{L}^T$  in equation 3 is not the inverse of the forward modeling operator, the computed migration image  $\mathbf{m}_{mig}$  is a blurred version of the true reflectivity model  $\mathbf{m}_0$ . Here, the blurring operator is defined as the  $\mathbf{L}^T \mathbf{L}$  operator in equation 3 or  $\Gamma(\mathbf{r}|\mathbf{r}_0)$  in equation 5, the blurring operator blurs the true reflectivity model  $\mathbf{m}_0$  to give the migration image  $\mathbf{m}_{mig}$  which often suffers from artifacts because of poor acquisition sampling and uneven illumination. The blurring can be mostly corrected by applying the inverse of  $\mathbf{L}^T \mathbf{L}$  to the migration image as

$$\mathbf{m}_0 = \overbrace{(\mathbf{L}^T \mathbf{L})^{-1}}^{\text{deblurring operator}} \mathbf{m}_{mig}. \quad (6)$$

However, computing the direct inverse of  $\mathbf{L}^T \mathbf{L}$  is computationally prohibitive for practical seismic imaging problems. One possible solution is iterative least-squares migration (Nemeth et al., 1999), which typically requires an order-of-magnitude more computations than standard migration. To accelerate the convergence, deblurring op-

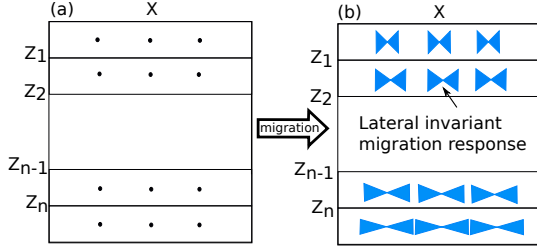


Figure 1: (a) Reference reflectivity model consisting of point scatterers and (b) migration image of the reference model. The migration responses for trial image points at the same depth location are assumed to be the same.

erators can be designed to approximate the inverse of the Hessian operator  $(\mathbf{L}^T \mathbf{L})^{-1}$ , which can then be used as a preconditioning operator (Hu et al., 2001; Guitton, 2004; Yu et al., 2006; Aoki and Schuster, 2009; Dai et al., 2009).

If the subsurface velocity model is laterally homogeneous and the recording aperture is sufficiently wide, the migration Green's function is approximately shift invariant in the horizontal direction, i.e., the migration responses for a point scatterer at the same depth  $z_i$  are same. As an example, it can be seen from Figure 1 that the migration responses for trial image points at the same depth location are same. Under this assumption equation 3 can be written as a 2D convolution in the  $x$ - and  $y$ - coordinates as (Hu et al., 2001):

$$m_{mig}(\mathbf{r}_0) = \int_{z_{min}}^{z_{max}} \int_{(x_0, y_0) \in \Omega} \Gamma(x - x_0, y - y_0, z | 0, 0, z_0) m(x, y, z_0) dx_0 dy_0 dz_0, \quad (7)$$

where  $\Omega$  denotes the horizontal coordinates in the model space,  $z_{min}$  and  $z_{max}$  represents the lower and upper vertical boundary of the assumed lateral homogeneous medium. Applying a 2D Fourier transform in  $x$ - and  $y$ - to equation 7 gives

$$\hat{m}_{mig}(k_x, k_y, z) = \int_{z_{min}}^{z_{max}} \hat{\Gamma}(k_x, k_y, z | 0, 0, z_0) \hat{m}(k_x, k_y, z_0) dz_0, \quad (8)$$

where the caret indicates a function in the wavenumber-space domain. The final deblurred image  $\hat{m}(x, y, z)$  can be obtained by first applying the inverse operator  $[\int_{z_{min}}^{z_{max}} \hat{\Gamma}(k_x, k_y, z_0 | 0, 0, z_0) dz_0]^{-1}$  to the migration image  $\hat{m}_{mig}(k_x, k_y, z)$  and then taking the inverse Fourier in the  $x$ - and  $y$ - coordinates (Yu et al., 2006).

However, this method assumes a  $v(z)$  medium, which means that the deconvolution operators are horizontally invariant. To account for lateral variations in the velocity model, Hu et al. (2001) and Yu et al. (2006) developed migration deconvolution filters for large overlapping patches in the model, and blended them together to get MD filters for laterally invariant media.

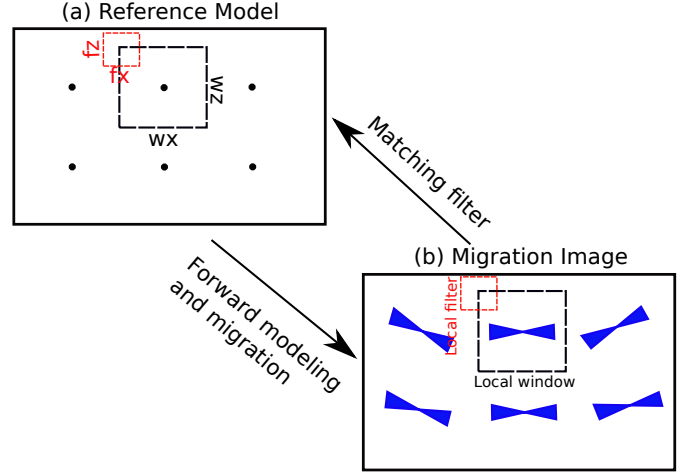


Figure 2: Illustration of local matching filters that transform the migration image to its reference model.

As an alternative, Guitton (2004) and Aoki and Schuster (2009) proposed localized deblurring filters which deblur the migration image in the space domain. The deblurring filter is estimated using a reference model and its migration image. Following Aoki and Schuster (2009), the reference reflectivity model is constructed using a uniform distribution of point scatterers as shown in Figure 2a. The reference data  $\mathbf{d}_{ref}$  are generated from these reference reflectivity and background velocity models, which are then migrated to get a reference migration image  $\mathbf{m}_{mig-ref}$  as

$$\mathbf{m}_{mig-ref} = \mathbf{L}^T \mathbf{L} \mathbf{m}_{ref} = \mathbf{L}^T \mathbf{d}_{ref}. \quad (9)$$

As shown in Figure 2,  $\mathbf{m}_{ref}$  and  $\mathbf{m}_{mig-ref}$  are divided into subdomains. A subdomain or a local window is chosen such that a point scatterer is at the center of the window. Within the local window, the migration Green's function can be assumed constant. The deblurring filter for each local window is then estimated by locally matching the reference migration image with the true reference reflectivity model as (Dai et al., 2011)

$$\mathbf{F}_i * [\mathbf{m}_{ref-mig}]_i = [\mathbf{m}_{ref}]_i, \quad (10)$$

where  $i$  indicates the  $i$ th local window and  $[\mathbf{m}_{mig-ref}]_i$  and  $[\mathbf{m}_{ref}]_i$  denotes the reference migration image and the reference reflectivity model within the local window. Same as the localized migration Green's function, each deblurring filter is also constant within its corresponding local window.

Since convolution operation is commutative, so that

$$\mathbf{F}_i * [\mathbf{m}_{ref-mig}]_i = [\mathbf{m}_{ref-mig}]_i * \mathbf{F}_i, \quad (11)$$

This means that the reference migration image in the local window (shown as the black dashed square in Figure 2) can be formulated as a convolution matrix  $\mathbf{M}_{ref-mig}$  with size of  $(N + M - 1) \times N$  and the corresponding small local deblurring filter (shown as the red dash square in Figure

2) can be reformed into a vector  $\mathbf{f}$  with size of  $N \times 1$ , where  $N = fx \times fz$  and  $M = wx \times wz$ .  $fx$  and  $fz$  is the filter length in horizontal and vertical direction, respectively.  $wx$  and  $wz$  is the window size in horizontal and vertical direction, respectively. Therefore we can rewrite equation 10 in matrix-vector notation as

$$[\mathbf{M}_{ref\_mig}]_i \mathbf{f}_i = [\mathbf{m}_{ref}]_i, \quad (12)$$

where now  $[\mathbf{m}_{ref}]_i$  is the vector form of the reference reflectivity model in the same window with size of  $(N + M - 1) \times 1$ . Multiply  $[\mathbf{M}_{ref}]_i^T$  on both side of equation 12 changes it to the form of normal equation

$$[\mathbf{M}_{ref\_mig}]_i^T [\mathbf{M}_{ref\_mig}]_i \mathbf{f}_i = [\mathbf{M}_{ref\_mig}]_i^T [\mathbf{m}_{ref}]_i. \quad (13)$$

The unknown deblurring filters can be achieved by solving this normal equation with LU decomposition method, which approximate the inverse of the Hessian within the local window.

## Deblurring filters in a viscoacoustic medium

Previous MD research concentrated on assuming a lossless media. However, strong subsurface attenuation can significantly distort the amplitudes and phases of seismic waves (Aki and Richards, 1980). To mitigate this problem, Q-LSRTM (Dutta and Schuster, 2014) was developed to generate migration images with more balanced amplitudes and accurately positioned reflectors than standard migration techniques. However, the inverted images from Q-LSRTM sometimes tend to have lower resolution when compared to the benchmark acoustic LSRTM images because the adjoint Q propagators used for backpropagating the data residual during Q-LSRTM are also attenuative.

This loss in resolution can be explained by analyzing the migration Green's function for a viscoacoustic media. For a homogeneous medium with velocity  $v_0$  and a monochromatic point source at  $\mathbf{r}_s = (x_s, z_s)$  with angular frequency  $\omega$ , the acoustic Green's function  $G(\mathbf{r}, \mathbf{r}_s)$  is given by

$$G(\mathbf{r}, \mathbf{r}_s) = \frac{\exp\{i\omega \frac{|\mathbf{r}_s - \mathbf{r}|}{v_0}\}}{|\mathbf{r}_s - \mathbf{r}|}. \quad (14)$$

If the medium is lossy, the viscoacoustic Green's function can be derived by replacing the acoustic phase-velocity  $v_0$  with the complex phase velocity given by (Aki and Richards, 1980):

$$v(\omega) = v_0 \left[ 1 + \frac{1}{\pi Q} \ln \frac{\omega}{\omega_0} \right] \left( 1 - \frac{i}{2Q} \right). \quad (15)$$

where  $Q$  is the quality factor which is used to describe the attenuative of the subsurface medium and  $\omega_0$  is the reference reference frequency. After substituting equation 15 into equation 14, we get the viscoacoustic Green's function as

$$G(\mathbf{r}, \mathbf{r}_s) = \exp\left\{ \overbrace{\frac{i\omega |\mathbf{r}_s - \mathbf{r}|}{v_0 \xi}}^{\text{phase distortion}} \right\} \exp\left\{ -\overbrace{\frac{\omega |\mathbf{r}_s - \mathbf{r}|}{2Q v_0 \xi}}^{\text{amplitude/frequency attenuation}} \right\}, \quad (16)$$

where  $\xi = [1 + \frac{1}{\pi Q} (\ln(\frac{\omega}{\omega_0}))][1 + \frac{1}{4Q^2}]$ . The first exponential term is the phase distortion term and the second exponential term represents the amplitude/high-frequency loss term. Therefore, the viscoacoustic and acoustic migration Green's function are given by

$$\Gamma_Q = \frac{\exp\{i \frac{\omega}{v_0 \xi} (rr - rr_0)\} \exp\{-\frac{\omega}{2Q v_0 \xi} (rr + rr_0)\}}{rr \cdot rr_0}, \quad (17)$$

$$\Gamma_{acou} = \frac{\exp\{i \frac{\omega}{v_0} (\frac{rr}{\xi} - rr_0)\} \exp\{-\frac{\omega}{2Q v_0 \xi} (rr)\}}{rr \cdot rr_0}, \quad (18)$$

where  $rr = |\mathbf{r}_s - \mathbf{r}| + |\mathbf{r}_g - \mathbf{r}|$  and  $rr_0 = |\mathbf{r}_s - \mathbf{r}_0| + |\mathbf{r}_g - \mathbf{r}_0|$ . Equation 18 shows that if acoustic migration is used to migrate viscoacoustic data, the reflection energy will be focused at the wrong subsurface location  $\frac{rr}{\xi} = rr_0$ , instead of  $rr_0$ . However, if viscoacoustic migration (Q-RTM) is used, the reflector will be imaged at the right subsurface location  $rr_0$ . However, the backward propagated receiver wavefield in Q-RTM is further attenuated because of the  $\exp\{-\frac{\omega}{2Q v_0 \xi} (rr_0)\}$  term on the RHS in equation 16. Thus, images from Q-LSRTM will have lower resolution when compared to the images computed by acoustic LSRTM on acoustic data.

To increase the resolution of the Q-LSRTM image and accelerate the convergence of the least-squares iterations, we propose the use of local viscoacoustic deblurring filters. Similar to the way we estimate the acoustic deblurring filter, an evenly distributed point scatterer model is chosen as the reference reflectivity model. The viscoacoustic synthetic data  $\mathbf{d}_{Q\_ref}$  are generated using this reference reflectivity model and the background velocity and Q model. The data are then migrated by Q-RTM to obtain a reference Q-RTM image. Viscoacoustic deblurring filters for different subsection of the Q-RTM image are then estimated using matching filters as described in the previous section. The viscoacoustic deblurring filters at  $i$ th window (or subsection) are estimated in the space domain by solving the system of equations given by

$$[\mathbf{F}_Q]_i * (\mathbf{L}_Q^T \mathbf{d}_{Q\_ref})_i \approx [\mathbf{m}_{ref}]_i. \quad (19)$$

As the reference migration image is generated from the same source-receiver configuration as the original field experiment and by using the same velocity and Q models, the application of these deblurring filters to the migration image is an acceptable approximation to the true inverse Hessian operator  $\mathbf{L}_Q^T \mathbf{L}_Q$ .

## Q-LSRTM using viscoacoustic deblurring filters

The misfit function for Q-LSRTM is given by (Dutta and Schuster, 2014)

$$\epsilon = \frac{1}{2} \|\mathbf{L}_Q \mathbf{m}^{(k)} - \mathbf{d}_Q^{obs}\|^2, \quad (20)$$

where  $\mathbf{d}_Q^{obs}$  denotes the observed data that have suffered from attenuation,  $\mathbf{m}^k$  represents the migration image at the  $k^{th}$  iteration and  $\mathbf{L}_Q$  is the linearized viscoacoustic forward modeling operator. The Gauss-Newton gradient for this misfit function is given by

$$(\mathbf{L}_Q^T \mathbf{L}_Q) \Delta \mathbf{m}^{(k)} = \mathbf{L}_Q^T [\mathbf{L}_Q \mathbf{m}^{(k)} - \mathbf{d}_Q^{obs}] = \mathbf{g}^{(k)}. \quad (21)$$

It can be seen from this equation that the update at each iteration  $\mathbf{g}^{(k)}$  is a blurred version of the desired update  $\Delta \mathbf{m}^{(k)}$ . The blurring is because of the viscoacoustic migration Green's function  $\mathbf{L}_Q^T \mathbf{L}_Q$ . Thus, a preconditioner for the gradient in equation 21 can be written as the deblurring approximation  $[\mathbf{L}_Q^T \mathbf{L}_Q]^{-1} \approx \mathbf{f}_Q$ , so that the preconditioned gradient in equation 21 can be used in the iterative update equation

$$\mathbf{m}^{(k+1)} = \mathbf{m}^{(k)} - \alpha \mathbf{F}_Q * (\mathbf{L}_Q^T (\mathbf{L}_Q \mathbf{m}^{(k)} - \mathbf{d}_Q^{obs})), \quad (22)$$

Here  $\alpha$  is the step length.

## NUMERICAL RESULTS

The effectiveness of Q-LSRTM with viscoacoustic deblurring filters is now demonstrated with synthetic data generated from the Marmousi II model, the benchmark viscoacoustic data released by Schlumberger for the BP2004Q model and field data recorded in a crosswell experiment in Friendswood, Texas. The data are migrated using acoustic RTM, acoustic LSRTM, Q-RTM, Q-LSRTM and Q-LSRTM with viscoacoustic deblurring filters. The migration results in the same figure are compared at the same colorbar scale.

### Marmousi II model

The preconditioned Q-LSRTM method is first tested on the Marmousi II model. Figure 3 shows the true velocity and Q models, respectively, used for generating the observed data. The Q model is chosen such that the attenuation layers overly the deeper anticlines. We use time-domain viscoacoustic finite-difference modeling algorithm with one standard linear solid model for both data simulation and migration. A Ricker wavelet with a peak frequency of 15 Hz is used as the source wavelet. A fixed-spread acquisition geometry is used where there are 150 sources evenly distributed on the surface at an interval of 50 m. The data are recorded by 800 receivers for each shot uniformly distributed every 10 m on the surface.

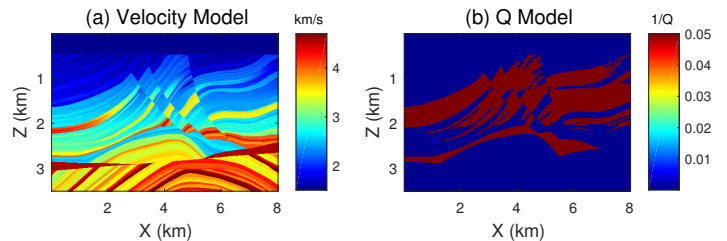


Figure 3: The Marmousi model: (a) true velocity model and (b) true Q model.

Conventional acoustic RTM and LSRTM images obtained from the viscoacoustic data are shown in Figures 4a and 4b, respectively. Both these images fail to recover the amplitudes of the reflectors at the deeper parts. The Q-LSRTM image, shown in Figure 4d, shows improvement in the deeper layers when compared to the acoustic migration results. However, the Q-LSRTM image has lower resolution for the reflectors below the Q anomaly when compared to the benchmark acoustic LSRTM image, shown in Figure 4f, that has been obtained from acoustic data generated using the same velocity model in Figure 3a. As discussed in the previous section, this low resolution problem with Q-LSRTM is due to the attenuation properties of the adjoint operator  $\mathbf{L}_Q^T$ . However, the preconditioned Q-LSRTM image in Figure 4e obtained using viscoacoustic deblurring filters has better resolution when compared to the Q-LSRTM image in Figure 4d. The amplitudes in the preconditioned Q-LSRTM image are also better balanced when compared to the acoustic RTM and LSRTM images in Figures 4a and 4b, respectively. The magnified views of these images are compared in Figures 5 and 6. The black arrows in these figures point to the areas in which noticeable improvements in the resolution can be seen. Figure 5e shows the wavenumber spectrum of a vertical slice at  $x = 3.11$  km in Figure 5. The wavenumber spectrum clearly shows the improvement in resolution with preconditioned Q-LSRTM. Figure 6e shows the wavenumber spectrum of a vertical slice at  $x = 5.13$  km in Figure 6. It is evident from these plots that the high-wavenumber details in the image are successfully recovered in the preconditioned Q-LSRTM image and these images have a similar resolution as the benchmark image obtained from using acoustic LSRTM on acoustic data.

The residual as a function of iteration number for LSRTM, Q-LSRTM and preconditioned Q-LSRTM is plotted in Figure 7. The convergence rate for preconditioned Q-LSRTM is much faster than Q-LSRTM especially at first several iterations. The residuals in the 3rd and 9th iteration of preconditioned Q-LSRTM are almost equal to the residuals in the 6th and 20th iterations of Q-LSRTM, respectively. Thus, a speedup of around 50% can be seen with the proposed preconditioning method. The convergence rate for preconditioned Q-LSRTM is better than that of standard Q-LSRTM because the Hessian effect is accounted for by the viscoacoustic deblurring filters.

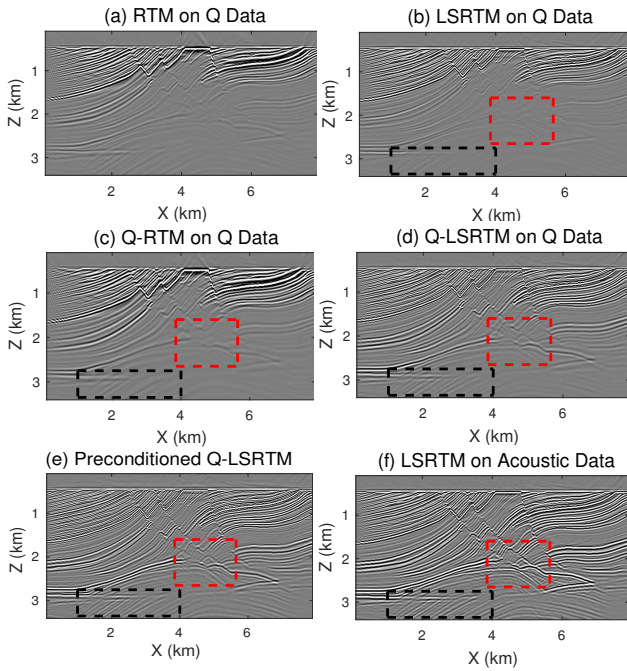


Figure 4: Comparison between images on viscoacoustic data from (a) acoustic RTM, (b) acoustic LSRTM, (c) Q-RTM, (d) Q-LSRTM, (e) Q-LSRTM using viscoacoustic deblurring filters as a preconditioner, 20 least-squares iterations are carried out in all cases. (f) Acoustic LSRTM on acoustic data, which is used as benchmark image.

## BP viscoacoustic benchmark data

The preconditioned Q-LSRTM method is now tested on the B2004Q dataset generated by Schlumberger (Billette and Brandsberg-Dahl (2005); Cavalca et al. (2013)). The velocity and Q models used for migration are shown in Figures 8a and 8b, respectively. The observed data are generated using a Ricker wavelet with a peak frequency of 19Hz. The original dataset has 1348 shots and each shot is recorded by 2401 receivers. The shot spacing is 50 m while the receivers are distributed on both sides of a shot at a spacing of 12.5 m. The sources and receivers are placed at a depth of 12.5 m.

For our numerical tests, we only use 236 shots. The true reflectivity model, shown in Figure 9f, is used to compare the acoustic and Q-LSRTM images. In the acoustic LSRTM image in Figure 9b, it is difficult to delineate the reflectors near the salt flank. The Q-LSRTM image, shown in Figure 9d, has better balanced amplitudes than the acoustic LSRTM image. However, the preconditioned Q-LSRTM image in Figure 9e has reflectors with better balanced amplitudes and better resolution than the standard Q-LSRTM and the acoustic LSRTM images. Magnified views of these images, shown in Figure 10a-10d, also illustrate the same. Figure 10e shows the wavenumber spectrum of a vertical slice at  $x = 17.05$  km in Figure 10. The brown curve which represent the spectrum of

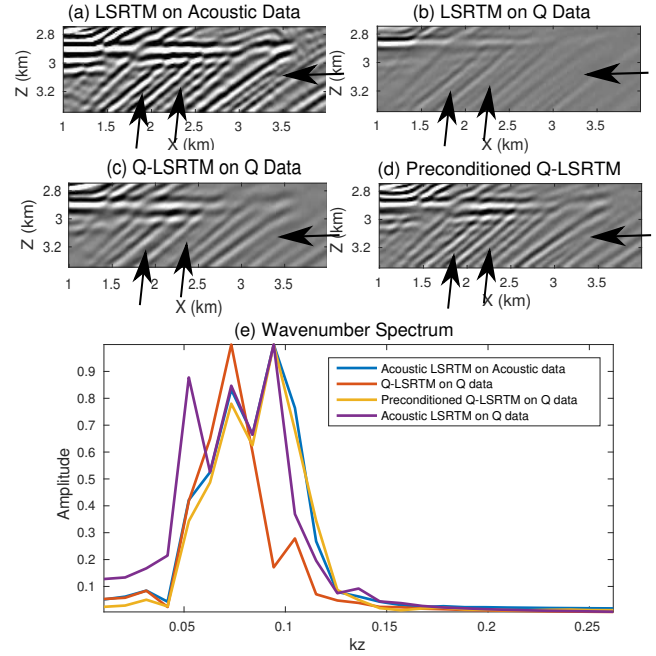


Figure 5: Magnified views of the black boxes in Figure 4. The black arrows point to the areas in which improvements can be seen. Figure 5e shows the wavenumber spectrum of a vertical slice at  $x = 3.11$  km in above four pictures.

the preconditioned Q-LSRTM image clearly shows an improvement in resolution when compared with Q-LSRTM indicated by the blue line.

The zoomed views also reveal some artifacts parallel to the salt boundary that got amplified in the preconditioned Q-LSRTM image. When observed carefully, these artifacts can also be seen in the acoustic RTM and LSRTM images. The residual as a function of iteration number for LSRTM, Q-LSRTM and preconditioned Q-LSRTM is plotted in Figure 11. The convergence rate for preconditioned Q-LSRTM is much faster than Q-LSRTM and acoustic LSRTM especially for the first few iterations.

## Friendswood crosswell field data

As a final example, we test our preconditioned Q-LSRTM method on the Friendswood crosswell field dataset. Two 305-m-deep cased wells separated by 183 m were used as the source and receiver wells. Downhole explosive source of 10-g charges were fired at intervals of 3 m from 305 m to 9 m in the source well, the receiver well had 96 receivers placed at depths ranging from 293 m to 3 m. The data were recorded with a sampling interval of 0.25 ms for a total recording time of 0.375 s (Chen et al., 1990). During processing, the data are Wiener-filtered to transform the original wavelet to a Ricker wavelet with a 200-Hz peak frequency. The migration velocity and Q models are shown in Figures 12a and 12b, respectively. The migration velocity model is estimated by early-arrival waveform

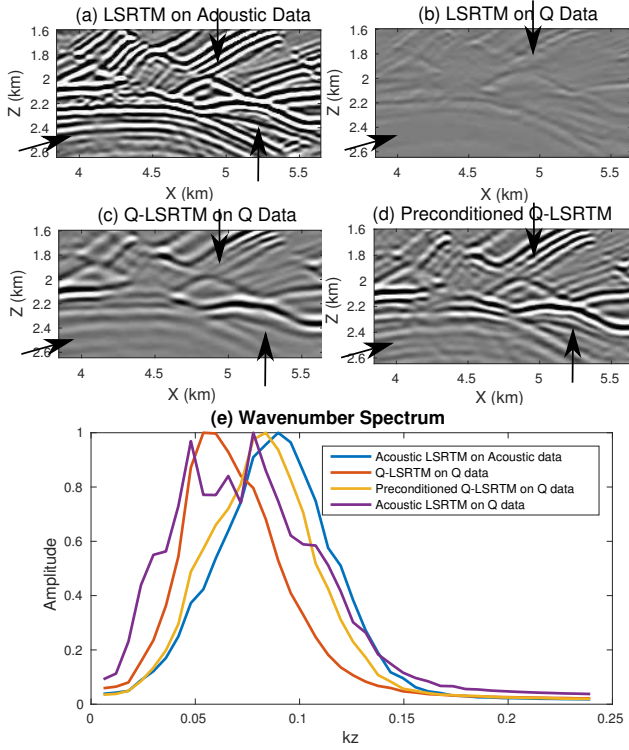


Figure 6: Magnified views of the red boxes in Figure 4. The black arrows point to the areas in which improvements can be seen. Figure 6e shows the wavenumber spectrum of a vertical slice at  $x = 5.13$  km in above four pictures.

inversion and the migration Q model is estimated by a wave-equation Q tomography (Dutta and Schuster, 2016)

The comparison between the acoustic LSRTM and Q-LSRTM images after 20 iterations are shown in Figure 13a and 13b, respectively. Similar to the synthetic examples, the amplitudes are more balanced in the Q-LSRTM image in Figure 13d than in the acoustic RTM and LSRTM images in Figure 13a and 13b, respectively. While the resolution becomes lower. The preconditioned Q-LSRTM image is shown in Figure 13e. When compared to the standard Q-LSRTM image, the preconditioned LSRTM image has better resolution at depths of 10-80 m. Magnified views of these areas are shown in Figure 14 that further validate the improvement in resolution with our proposed preconditioning method. The black arrows in these figures depict the areas that have become clearer in the preconditioned Q-LSRTM image.

As a sanity check, reflectivity slices from the preconditioned Q-LSRTM image are compared to the well log data taken at a distance of 12 m from the source well. The comparison between the well log profile and the standard Q-LSRTM and the preconditioned Q-LSRTM reflectivity profiles are shown in Figure 15a and 15b, respectively. It is evident from this figure that the well log agrees better with the preconditioned Q-LSRTM image than with

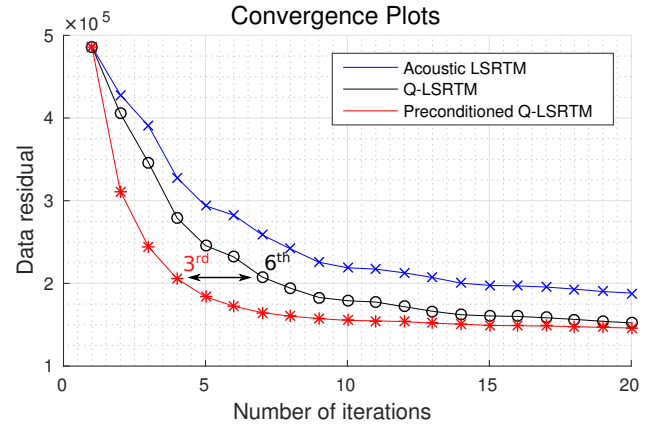


Figure 7: Convergence curve for acoustic LSRTM, Q-LSRTM and preconditioned Q-LSRTM for the Marmousi II model.

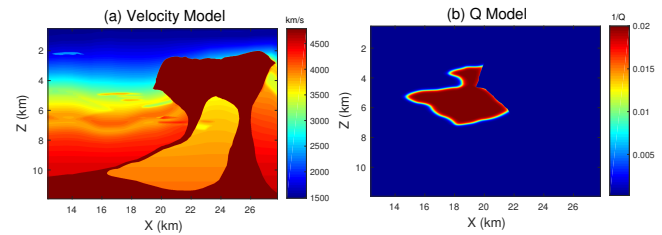


Figure 8: BP2004Q model: (a) true velocity model and (b) true Q model.

the Q-LSRTM images. The black arrows in this figure highlight the same.

## CONCLUSIONS

A preconditioned Q-LSRTM method is presented that uses viscoacoustic deblurring filters to compensate for the amplitude and resolution loss due to strong subsurface attenuation. Numerical tests on synthetic and field data validate that the proposed preconditioning method mitigates the problem of low resolution associated with standard Q-LSRTM and can produce images with better balanced amplitudes and better resolution than acoustic RTM and LSRTM. The viscoacoustic deblurring filters are estimated from a reference model with evenly distributed point-scatterers and its Q-RTM image using local matched filters. The proposed preconditioning method is also shown to improve the convergence rate of the least-squares iterations by more than 30 percent in some cases. Similar to standard Q-LSRTM, a fairly accurate estimation of the background Q model is required to see noticeable improvements in the image quality with the proposed preconditioned Q-LSRTM method.

## ACKNOWLEDGMENTS

The research reported in this paper was supported by the King Abdullah University of Science and Technology

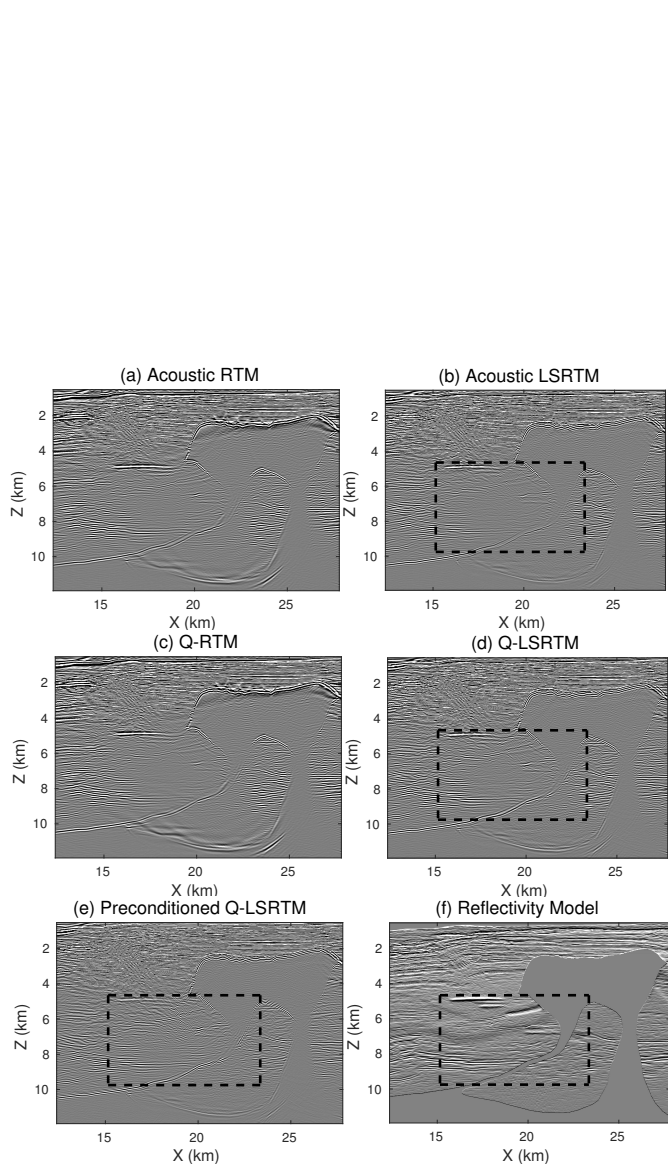


Figure 9: Comparison between images from (a) acoustic RTM, (b) acoustic LSRTM, (c) Q-RTM, (d) Q-LSRTM, (e) preconditioned Q-LSRTM and (f) the true reflectivity model. The black boxes indicate the areas for the magnified views.

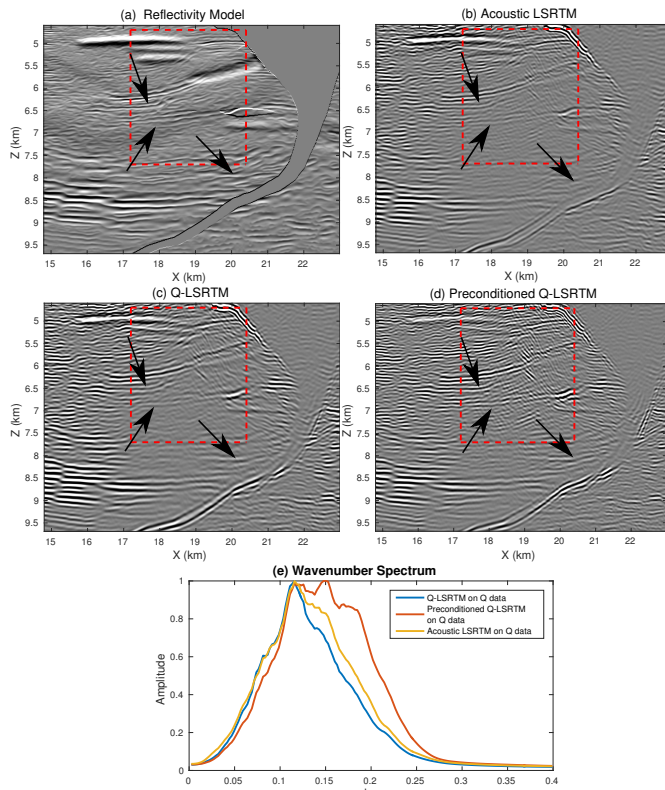


Figure 10: Magnified views of the black boxes in Figure 9. The black arrows point to the reflectors below the high attenuation area where improvements from the preconditioned Q-LSRTM method can be seen. Figure 10e shows the wavenumber spectra of a vertical slice at  $x = 17.05$  km in above four pictures.

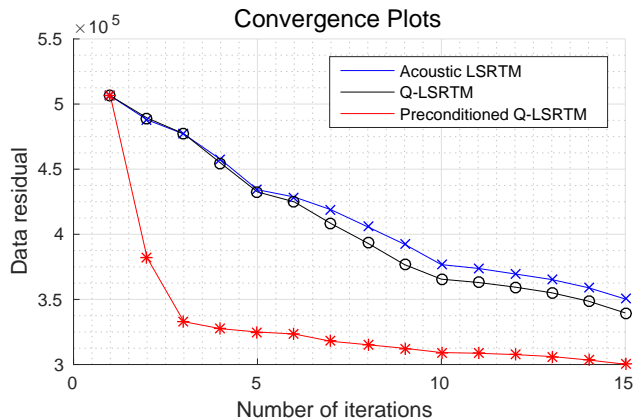


Figure 11: Convergence curve for LSRTM, Q-LSRTM and Preconditioned Q-LSRTM for the BP2004Q benchmark data.

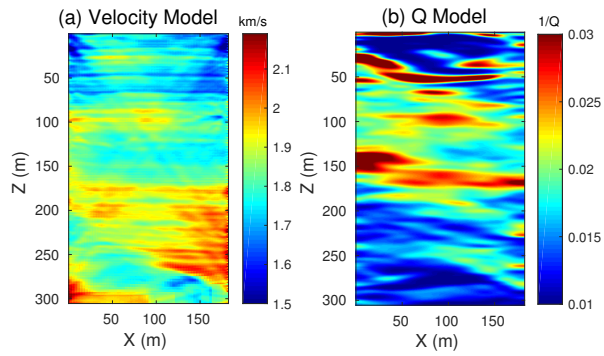


Figure 12: (a) The estimated migration velocity and (b) Q models for the Friendswood crosswell dataset.

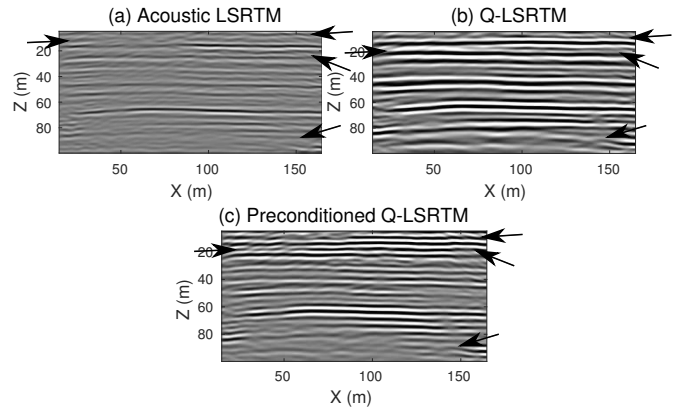


Figure 14: Magnified views of the black boxes in Figure 13. The black arrows point to the reflectors where the improvement in resolution can be seen from the preconditioned Q-LSRTM method.

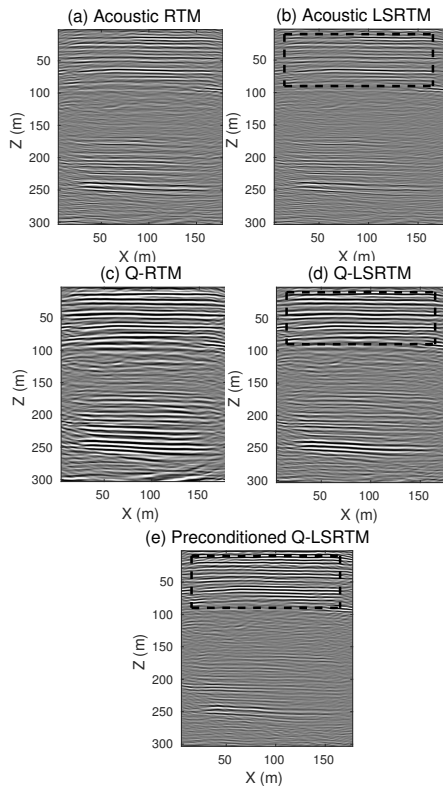


Figure 13: Comparison between images from (a) acoustic RTM, (b) acoustic LSRTM, (c) Q-RTM, (d) Q-LSRTM and (e) preconditioned Q-LSRTM. 20 least-squares iterations are carried out in all the cases.

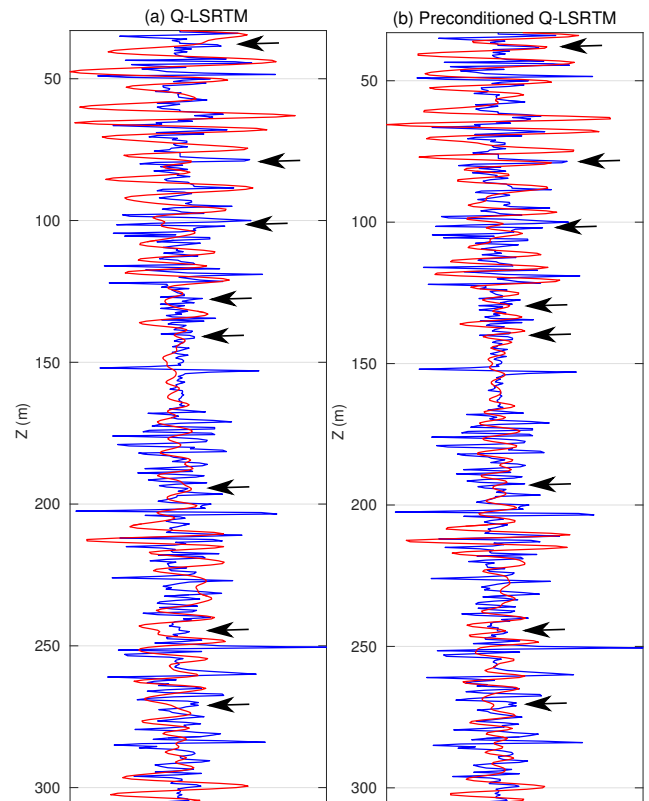


Figure 15: Comparison between the true reflectivity obtained from a well log (represented by the blue line) and the inverted reflectivity (represented by the red line) from (a) Q-LSRTM and (b) preconditioned Q-LSRTM. The well log is at a distance of 12 m from the source well

(KAUST) in Thuwal, Saudi Arabia. We are grateful to the sponsors of the Center for Subsurface Imaging and Modeling (CSIM) Consortium for their financial support. For computer time, this research used the resources of the Supercomputing Laboratory at KAUST. We thank them for providing the computational resources required for carrying out this work. We also thank Schlumberger and BP for providing the BP2004Q dataset and Exxon for the Friendswood crosswell data.

## REFERENCES

- Aki, K., and P. G. Richards, 1980, *Quantitative seismology*: Freeman Publication Co., San Francisco.
- Aoki, N., and G. T. Schuster, 2009, Fast least-squares migration with a deblurring filter: *Geophysics*, **74**, WCA83–WCA93.
- Billette, F., and S. Brandsberg-Dahl, 2005, The 2004 bp velocity benchmark.
- Cavalca, M., R. Fletcher, M. Riedel, et al., 2013, Q-compensation in complex media—ray-based and wave-field extrapolation approaches: 2013 SEG Annual Meeting.
- Chen, S., L. Zimmerman, and J. Tugnait, 1990, Subsurface imaging using reversed vertical seismic profiling and crosshole tomographic methods: *Geophysics*, **55**, 1478–1487.
- Dai, N., G. F. West, et al., 1994, Inverse q migration: Presented at the 1994 SEG Annual Meeting, Society of Exploration Geophysicists.
- Dai, W., J. Schuster, et al., 2009, Least-squares migration of simultaneous sources data with a deblurring filter: Presented at the 2009 SEG Annual Meeting, Society of Exploration Geophysicists.
- Dai, W., X. Wang, and G. T. Schuster, 2011, Least-squares migration of multisource data with a deblurring filter: *Geophysics*, **76**, R135–R146.
- Dai, W., Z. Xu, R. Coates, et al., 2015, Least-squares reverse-time migration for visco-acoustic media.
- Dutta, G., and G. T. Schuster, 2014, Attenuation compensation for least-squares reverse time migration using the viscoacoustic-wave equation: *Geophysics*, **79**, S251–S262.
- , 2016, Wave-equation Q tomography (accepted): *Geophysics*.
- Fletcher, R., D. Nichols, and M. Cavalca, 2012, Wavepath-consistent effective q estimation for q-compensated reverse-time migration: Presented at the 74th EAGE Conference and Exhibition incorporating EUROPEC 2012.
- Guitton, A., 2004, Amplitude and kinematic corrections of migrated images for nonunitary imaging operators: *Geophysics*, **69**, 1017–1024.
- Hu, J., and G. T. Schuster, 1998, Migration deconvolution: SPIE’s International Symposium on Optical Science, Engineering, and Instrumentation, International Society for Optics and Photonics, 118–124.
- Hu, J., G. T. Schuster, and P. A. Valasek, 2001, Poststack migration deconvolution: *Geophysics*, **66**, 939–952.
- Jansson, P. A., and M. Richardson, 1997, Deconvolution of images and spectra: *Optical Engineering*, **36**, 3224–3225.
- Nemeth, T., C. Wu, and G. T. Schuster, 1999, Least-squares migration of incomplete reflection data: *Geophysics*, **64**, 208–221.
- Schuster, G. T., and J. Hu, 2000, Green’s function for migration: Continuous recording geometry: *Geophysics*, **65**, 167–175.
- Suh, S., K. Yoon, J. Cai, B. Wang, et al., 2012, Compensating visco-acoustic effects in anisotropic reverse-time migration: Presented at the 2012 SEG Annual Meeting, Society of Exploration Geophysicists.
- Sun, J., S. Fomel, T. Zhu, et al., 2015, Preconditioning least-squares rtm in viscoacoustic media by q-compensated rtm: Presented at the 2015 SEG Annual Meeting, Society of Exploration Geophysicists.
- Sun, J., S. Fomel, T. Zhu, and J. Hu, 2016, Q-compensated least-squares reverse time migration using low-rank one-step wave extrapolation: *Geophysics*, **81**, S271–S279.
- Valenciano, A., N. Chemingui, D. Whitmore, S. B. Dahl, et al., 2011, Wave equation migration with attenuation and anisotropy compensation: Presented at the 2011 SEG Annual Meeting, Society of Exploration Geophysicists.
- Wang, Y., 2007, Inverse-q filtered migration: *Geophysics*, **73**, S1–S6.
- Yu, J., J. Hu, G. T. Schuster, and R. Estill, 2006, Prestack migration deconvolution: *Geophysics*, **71**, S53–S62.
- Yu, Y., R. S. Lu, M. M. Deal, et al., 2002, Compensation for the effects of shallow gas attenuation with viscoacoustic wave-equation migration: *SEG Technical Program Expanded Abstracts*, **21**, 2062–2065.
- Zhang, Y., P. Zhang, H. Zhang, et al., 2010, Compensating for visco-acoustic effects in reverse-time migration: Presented at the 2010 SEG Annual Meeting, Society of Exploration Geophysicists.
- Zhu, T., and J. M. Harris, 2015, Improved seismic image by q-compensated reverse time migration: Application to crosswell field data, west texas: *Geophysics*, **80**, B61–B67.
- Zhu, T., J. M. Harris, and B. Biondi, 2014, Q-compensated reverse-time migration: *Geophysics*, **79**, S77–S87.